

ARTICLE OPEN



Abnormal nonlinear optical responses on the surface of topological materials

Haowei Xu¹, Hua Wang¹ and Ju Li^{1,2}✉

The nonlinear optical (NLO) responses of topological materials are under active research. Most previous works studied the surface and bulk NLO responses separately. Here we develop a generic Green's function framework to investigate the surface and bulk NLO responses together. We reveal that the topological surface can behave disparately from the bulk under light illumination. Remarkably, the photocurrents on the surface can flow in opposite directions to those in the bulk interior, and the light-induced spin current on the surface can be orders of magnitude stronger than its bulk counterpart on a per-volume basis. We also study the responses under inhomogeneous field and higher-order NLO effect, which are all distinct on the surface. These anomalous surface responses suggest that light can be a valuable tool for probing the surface states of topological materials. Besides, the surface effects should be prudently considered when investigating the optical properties of topological materials.

npj Computational Materials (2022)8:1111; <https://doi.org/10.1038/s41524-022-00782-y>

INTRODUCTION

In recent years, nonlinear optical (NLO) effects such as the bulk photovoltaic (BPV) effect have attracted substantial interest, owing to their potential applications in e.g., photodetection^{1–4}, energy harvesting^{5–10}, and material characterization^{11–14}. The interplay between topology and NLO properties is particularly intriguing. Certain NLO effects are closely related to topological quantities such as the Berry curvature and quantum metric tensors, thus the NLO responses can be utilized as a probe of these bulk topological properties^{11–13,15–19}. On the other hand, the topological nature can boost the NLO responses^{2,20,21}, thus the efficiency of applications such as photodetection could be enhanced by using topological materials.

Regarding NLO properties in topological materials, most works hitherto studied the bulk^{1–4,11–29} and surface^{30–36} responses separately. Only a few works studied the NLO responses of the surface and bulk together. Actually, even in normal materials, the surface and bulk responses can be substantially different. A typical example is that surface naturally breaks the inversion symmetry, which forbids even-order responses. Hence even-order responses are always allowed on the surfaces, even if the bulk possesses inversion symmetry. In addition, in topological insulators, when the Fermi level is within the bulk bandgap, some NLO responses are zero in the bulk when the light frequency is below the bulk bandgap. In contrast, the surface always has non-zero responses due to the gapless topological surface states. These considerations necessitate careful inspections of the surface effects in NLO processes. Typically, a slab model with finite thickness is used to study the surface effects. This approximate model omits a few essential interactions: the surface electrons should interact with all the bulk electrons, and the bulk should be (nearly) infinite in depth in many experimental scenarios. Besides these concerns pertinent to surface effects, previous studies on the NLO effects are mostly based on the non-interacting single-particle framework (independent particle approximation), and the many-body effects are ignored. Indeed, many-body effects such as electron-phonon

coupling^{37,38}, excitonic effect^{39,40}, and strong correlations⁴¹ can greatly influence the optical responses.

In this work, we develop a generic many-body framework for computing the NLO effects based on the Green's function formalism, which can naturally incorporate various many-body effects. In the Supplementary Note 2.4, we study strong electron-electron correlations as an example to showcase the merit of the Green's function framework. Besides second-order responses such as BPV, our Green's function formalism can be systematically and conveniently extended to handle higher-order NLO effects and inhomogeneous light fields. We apply our framework to the surface states of topological materials, whose Green's functions are obtained with the iterative Green's function (IGF) method^{42,43}. This approach enables a rigorous treatment of the surface-bulk interactions. We take type-II Weyl semimetal T_d -WTe₂^{44,45} as an example. The bulk of T_d -WTe₂ is non-centrosymmetric and gapless, which is similar to the surface from a symmetry or bandgap point of view. However, the NLO responses on the surface are distinct from those in the bulk interior. Specifically, the BPV charge current on the surface and in the bulk can flow in opposite directions (Fig. 1). This striking behavior demonstrates that surface effects in topological materials can be significant. We clarify that this is mainly a topological effect and can be absent in normal materials. Also, the surface bulk spin photovoltaic (BSPV)^{46,47} conductivity is colossal and can be larger than its bulk counterpart by a factor of 10 on a per-volume basis. Hence the surface of topological materials can be efficient platforms for spintronics applications, particularly when 2D materials or nanoscale thin films are required. In addition, we show that the responses under inhomogeneous fields and higher-order NLO effects are all distinct between the surface and the bulk. These anomalous responses on the surfaces indicate that the NLO effects can be utilized to probe the surface atomic structure. On the other hand, the surface responses should be prudently considered when investigating the NLO properties of topological materials. This is particularly important when the penetration depth of the light is shallow or when the material is thin, like less than 10^2 monolayers

¹Department of Nuclear Science and Engineering, Massachusetts Institute of Technology, Cambridge, MA 02139, USA. ²Department of Materials Science and Engineering, Massachusetts Institute of Technology, Cambridge, MA 02139, USA. ✉email: liju@mit.edu

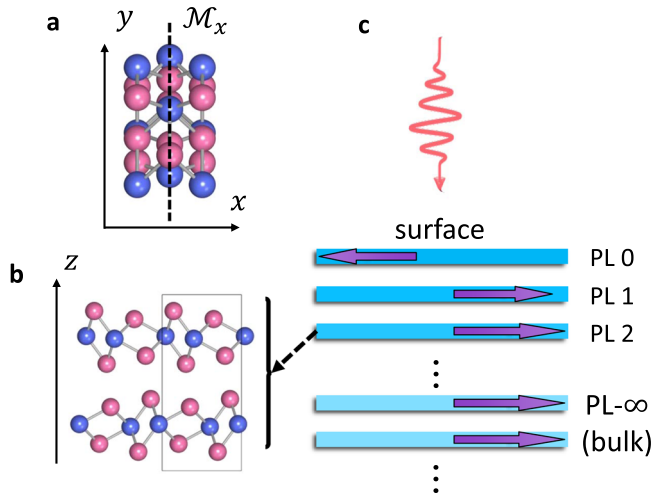


Fig. 1 Illustration of T_d - WTe_2 under light illumination. **a, b** Atomic structure of T_d - WTe_2 . The dashed line in **a** denotes the mirror- x symmetry \mathcal{M}_x of T_d - WTe_2 . **c** A sketch of materials under light illumination. The surface and bulk principal layer (PL) corresponds to PL-0 and PL- ∞ , respectively. The optical responses of the surface and the bulk can be distinct (indicated by the purple arrows). For T_d - WTe_2 , each PL consists of two WTe_2 layer without inversion symmetry as shown in **b**.

(~50 nm) thick. Given the semiconductor industry has generally moved to sub-10 nm technology nodes, now is an opportune time that such surface effects are addressed theoretically.

RESULTS

General theory

To calculate the responses under light, one needs the thermodynamic and quantum average of an observable θ , which can be formulated as⁴⁸

$$\langle \theta \rangle = -i \int \frac{d^d \mathbf{k}}{(2\pi)^d} \frac{dE}{2\pi} \text{Tr} \{ \theta G^<(\mathbf{k}, E) \}. \quad (1)$$

Here θ can be various observables, such as charge current ($\theta = -e\mathbf{v}$ with \mathbf{v} as the velocity operator), spin current [$\theta = \frac{1}{2}(\mathbf{v}\mathbf{s} + \mathbf{s}\mathbf{v})$ with \mathbf{s} as the spin operator], etc. $\int \frac{d^d \mathbf{k}}{(2\pi)^d}$ indicates the integration over the Brillouin zone in d -dimension. Tr is the trace operation. $G^<(\mathbf{k}, E)$ is the lesser Green's function and plays a role of energy-resolved distribution function. In non-interacting systems, one has $[G_0^<(\mathbf{k}, E)]_{mn} = 2\pi i \delta_{mn} f_m \delta(E - E_m)$, where m and n are band indices, and f_m and E_m are the occupation number and energy of band m at wavevector \mathbf{k} , respectively. In this case, one has $-i \int \frac{dE}{2\pi} [G_0^<(\mathbf{k}, E)]_{mn} = \delta_{mn} f_m$ and $\langle \theta \rangle = \int \frac{d^d \mathbf{k}}{(2\pi)^d} \sum_m \theta_{mm} f_m$, which is the usual thermal average of $\langle \theta \rangle$. When the electrons have interactions with phonon, defects, other electrons, etc., $G^<(\mathbf{k}, E)$ usually does not have a simple expression, but it can be obtained perturbatively with e.g., Feynman diagrams or non-perturbatively with other methods⁴⁸ [see Supplementary Note 2.4 for an example]. At equilibrium, the expectation of some observables, such as the charge current, should be zero. However, light can drive the system out of equilibrium, resulting in nonzero $\langle \theta \rangle$. Specifically, the interaction with light leads to a change in the lesser Green's function $\delta G^<$, which is dependent on the electric field \mathcal{E} . Then perturbatively one has $\langle \theta \rangle = A\mathcal{E} + B\mathcal{E}^2 + C\mathcal{E}^3 \dots$, where A , B and C correspond to the first-, second- and third-order optical response functions.

In the following, we use WTe_2 in its T_d phase (space group $Pmn2_1$, no. 31) as an example to study the NLO response on the

surface and in the bulk of topological materials. The atomic structure of T_d - WTe_2 is shown in Fig. 1. The lattice constants are $a = 3.48 \text{ \AA}$, $b = 6.28 \text{ \AA}$ and $c = 14.0 \text{ \AA}$. We define a Cartesian coordinate with x , y and z along the crystallographic a , b and c directions, respectively. T_d - WTe_2 is non-centrosymmetric, but has a mirror- x symmetry \mathcal{M}_x (dashed line in Fig. 1a). The unit cell of T_d - WTe_2 consists of two WTe_2 layers stacked along z direction (Fig. 1b), which is used as a principal layer (PL). Each PL has interactions with other PLs, and these interactions can be included in the equilibrium Green's function G_{PL}^0 using the IGF method^{42,43}. Electrons on each PL also have interactions with phonons, defects, etc. These interactions are implicitly represented by a phenomenological electron lifetime τ , which is taken to be a uniform value of 0.2 ps throughout this work unless explicitly stated. Under the current framework, the influence of τ is incorporated in the non-interacting Green's function as $G_0(E) = [E - H_0 + \frac{i\hbar}{\tau}]^{-1}$, where H_0 is the non-interacting single-particle Hamiltonian (Supplementary Note 3). The choice of $\tau = 0.2$ ps is based on experimental results and should be a conservative value^{49–53}. In Supplementary Note 5.1, we show how NLO responses vary with τ , and demonstrate that the main conclusions of our work remain valid for a wide range of τ . In order to demonstrate how our Green's function formalism can incorporate other many-body interactions, we also artificially add a Hubbard $U = 3$ eV term on the d orbitals of W atoms, and the Green's functions of this strongly correlated system are calculated with the dynamical mean field theory (DMFT)^{54–56}. We find that even with the artificial Hubbard U term, the main conclusions of our work remain valid (Supplementary Note 2.4).

The Green's function of each PL from the surface into the bulk can be obtained with the IGF method, and the PL-resolved responses, defined as the responses localized on each PL, can be obtained by putting G_{PL}^0 in the Green's function formalism (Methods). Specifically, the surface and the bulk correspond to PL-0 and PL- ∞ , whose Green's functions are denoted as $G_{\text{PL-0}}^0$ and $G_{\text{PL-}\infty}^0$, respectively (Fig. 1 PL- x denotes the x -th PL). In practice, G_{PL}^0 converges with $\text{PL} \gtrsim 20$, and we use $G_{\text{PL-50}}^0$ as the bulk Green's function ($G_{\text{PL-}\infty}^0 \simeq G_{\text{PL-50}}^0$). We fix the Fermi level E_F of T_d - WTe_2 so that it is charge neutral (no electron/hole doping) throughout this paper (Supplementary Fig. 13), and we study the optical responses in the mid-infrared regime ($\omega = 0.1 \sim 0.5$ eV). The spin-orbit coupling (SOC) is included for both the bulk and the surface.

Bulk photovoltaic effect

BPV effect indicates that in non-centrosymmetric materials, a DC charge current can be generated under photon illumination without any external bias voltage. The BPV effect can be expressed as

$$j^a = \sigma_{bc}^a(0; \omega, -\omega) \mathcal{E}^b(\omega) \mathcal{E}^c(-\omega), \quad (2)$$

where j^a is the current, while a and b/c are the directions of the current and the electric field, respectively. Here $\sigma_{bc}^a(0; \omega, -\omega)$ is the BPV conductivity and can be expressed as (Supplementary Note 2.1)

$$\begin{aligned} \sigma_{bc}^a(0; \omega, -\omega) &= -\frac{ie^2}{\omega^2} \sum_{\mathbf{k}} \int \frac{dE}{2\pi} \text{Tr} \{ v^a G^<(E) \}, \\ G^< &= G_0^r(E) v^b G_0^<(E + \omega) v^c G_0^a(E) \\ &\quad + G_0^r(E) v^b G_0^<(E + \omega) v^c G_0^a(E) \\ &\quad + G_0^<(E) v^b G_0^a(E + \omega) v^c G_0^a(E) \\ &\quad + (b \leftrightarrow c, \omega \leftrightarrow -\omega). \end{aligned} \quad (3)$$

One can see that the response operator θ in Eq. (1) has been taken as $-e\mathbf{v}$, which is the charge-current operator. G_0^r , G_0^a and $G_0^<$ are the retarded, advanced, and lesser Green's function of the system without light illumination, which are calculated with IGF. Here we assume that the light field is uniform. The \mathbf{k} arguments in Eq. (3)

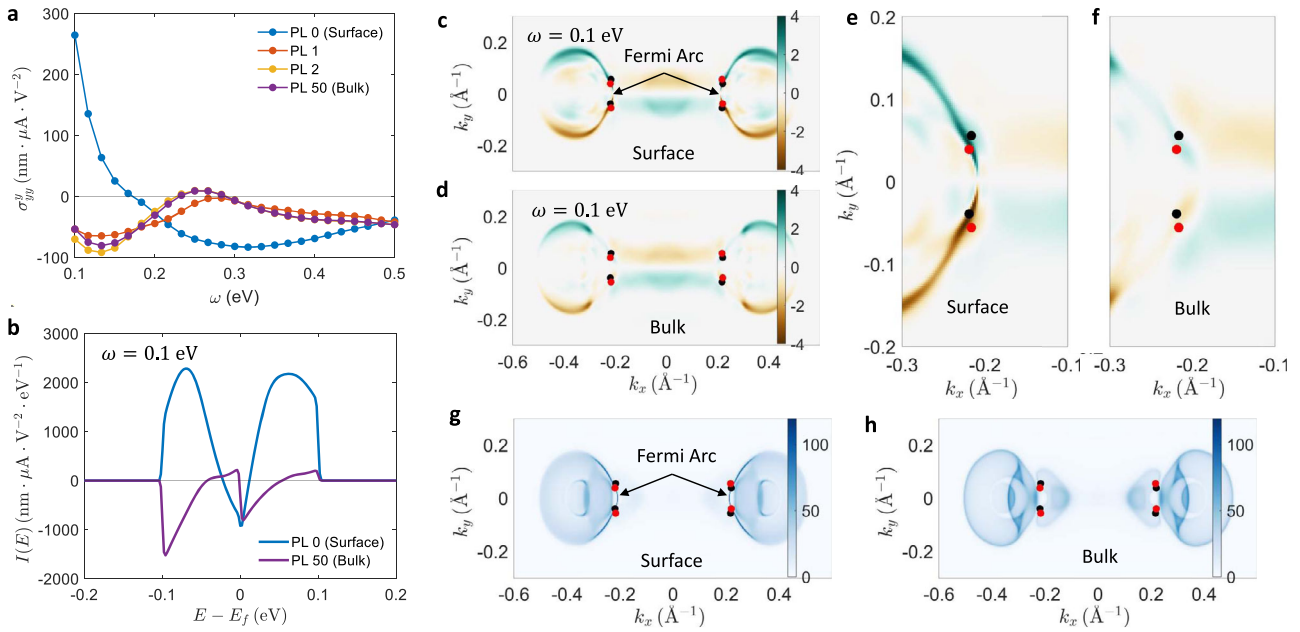


Fig. 2 BPV conductivity of T_d -WTe $_2$. **a** Layer resolved BPV conductivity for PLs from the surface to the bulk. **b** Energy-resolved contribution to the BPV conductivity for the surface and bulk PL for light frequency $\omega = 0.1$ eV. The energy-resolved contribution is defined as $I(E) \equiv -\frac{ie^3}{\omega^2 5} \sum_{\mathbf{k}} \text{Tr}\{v^a G^c(E)\}$. **c, d** \mathbf{k} -resolved contribution, defined as $I(\mathbf{k}, E) \equiv -\frac{ie^3}{\omega^2 5} \text{Tr}\{v^a G^c(\mathbf{k}, E)\}$ at $\omega = 0.1$ eV and $E = E_F$ for **(c)** surface PL and **(d)** bulk PL. **e, f** Same as **(c, d)**, but zoomed-in around the Fermi arc. **g, h** Spectrum function $A(\mathbf{k}, E)$ at $E = E_F$ for **(e)** surface and **(f)** bulk PL. The Fermi arcs are labelled by the arrows in **(c, e)**. In **(c–h)** the black and red dots mark the locations of Weyl points with $+1$ and -1 chirality, respectively.

are omitted for simplicity. S is the area of the unit cell. ($b \leftrightarrow c, \omega \leftrightarrow -\omega$) indicates the simultaneous exchange of b, c and $+\omega, -\omega$, which symmetrizes \mathcal{E}^b and \mathcal{E}^c .

The layer-resolved BPV conductivities of T_d -WTe $_2$ under linearly polarized light with y -polarization are shown in Fig. 2a. We show $\sigma(0; \omega, -\omega)$ for $\omega > 0.1$ eV because Eq. (3) has a spurious divergence as $\omega \rightarrow 0$, due to the $\frac{1}{\omega^2}$ factor. It is clear that the surface layer (PL-0) has distinct responses from the other PLs. The responses on the first (PL-1) and second (PL-2) are also different from those in the bulk, despite that the differences are less significant than those in the case of PL-0. This implies that the surface effects can penetrate three PLs, with a total thickness of around 5 nm. Remarkably, in some frequency region $\sigma_{\text{PL-0}}$ has the opposite sign to $\sigma_{\text{PL-1}}$ and $\sigma_{\text{PL-}\infty}$, indicating that under photon illumination, the local charge current would flow in opposite directions on PL-0. This is counter-intuitive, as PL-0 is directly attached to PL-1. Moreover, in some frequency regions $\sigma_{\text{PL-}\infty}$ is close to zero, while $\sigma_{\text{PL-0}}$ has a finite value, thus the current would flow mostly on the surface. The BPV conductivities under circularly polarized light are also distinct for the surface and the bulk (Supplementary Fig. 14). The BPV responses are closely related with geometric and topological properties^{15–17}. Thus, the layer-resolved NLO responses can be harnessed to probe and characterize the topological surface states. Another interesting observation is that the counter-propagating currents (Fig. 1) may lead to a magnetic field \mathbf{B} between PL-0 and PL-1, whose magnitude can be estimated using Ampère–Maxwell law as $\mathbf{B}(\mathbf{r}) \approx \frac{1}{2} \mu_0 \mathbf{j} \times \hat{\mathbf{d}}$, where μ_0 is the vacuum permittivity, \mathbf{j} is the current density on a single PL, \mathbf{r} is the spatial location, while $\hat{\mathbf{d}}$ is a unit vector that points from the PL to \mathbf{r} , and is perpendicular to the PL plane. Since $\mathbf{j} = \sigma \mathcal{E}^2$, the magnitude of the magnetic field is $|\mathbf{B}| \approx \frac{1}{2} \mu_0 |\mathbf{j}| = \frac{1}{2} \mu_0 \sigma \mathcal{E}^2 \sim 6.3 \times 10^{-4} \mathcal{E}^2$ [T], where σ is taken as $100 \text{ nm} \cdot \mu\text{A}/\text{V}^2$, and \mathcal{E} is in the unit of MV/cm. Note that this magnetic field \mathbf{B} has a pure orbital-magnetic origin, and the spin contribution is not

included. Specifically, an electric field of 1 MV/cm can generate a detectable interlayer magnetic field of 6 Gauss. In experiments, an electric field of 1 MV/cm is readily available and can be below the material damage threshold if pulsed lasers are used.

Next, we argue that the surface effects described above are mainly topological effects. First, we look at the \mathbf{k}, E -resolved contribution to σ in Eq. (3). The energy spectrum $I(E) \equiv -\frac{ie^3}{\omega^2 5} \sum_{\mathbf{k}} \text{Tr}\{v^a G^c(E)\}$ for $\omega = 0.1$ eV is plotted in Fig. 2b, where one can see that $I_{\text{PL-0}}(E)$ is generally different from $I_{\text{PL-}\infty}(E)$. Besides, although $G^c(E)$ should be nonzero for a wide range of E , $I(E)$ is nonzero only when $|E| \lesssim \omega$. This indicates that the shift current is essentially a resonant interband process: light with frequency ω can assist the electrons to transit from (\mathbf{k}, E) to $(\mathbf{k}, E \pm \omega)$, but due to the Pauli exclusion principle, such a transition is allowed only when $f_{\text{FD}}(E)[1 - f_{\text{FD}}(E \pm \omega)] > 0$, leading to $|E| \lesssim \omega$. Here f_{FD} is the Fermi–Dirac distribution. The \mathbf{k} -resolved contribution defined as $I(\mathbf{k}, E) \equiv -\frac{ie^3}{\omega^2 5} \text{Tr}\{v^a G^c(\mathbf{k}, E)\}$ reveals more detailed information on the surface effects. $I(\mathbf{k}, E)$ for $\omega = 0.1$ eV at the Fermi level $E = E_F$ is plotted in Fig. 2c, d. The difference between $I_{\text{PL-0}}(\mathbf{k}, E_F)$ and $I_{\text{PL-}\infty}(\mathbf{k}, E_F)$ is also significant, which can be inferred from the spectrum function defined as $A(\mathbf{k}, E) \equiv i \text{Tr}\{G_0^c(\mathbf{k}, E) - G_0^c(\mathbf{k}, E)\}$ (Fig. 2g, h). One can see that the difference between $I_{\text{PL-0}}(\mathbf{k}, E_F)$ and $I_{\text{PL-}\infty}(\mathbf{k}, E_F)$ lies largely in the region where the surface Fermi arc is located (labelled in Fig. 2c, g). This indicates that the difference between $\sigma_{\text{PL-0}}$ and $\sigma_{\text{PL-}\infty}$ is mainly from the topological surface states (see zoom-in plots around the Fermi arc in Fig. 2e, f). We have also examined $I(\mathbf{k}, E)$ for $E \neq E_F$, and found that it is generally different for PL-0 and PL-50 (see e.g., Supplementary Fig. 19), although after the integration over the Brillouin zone, $I(E)$ can be close in some E -regions, such as $E \sim E_F + 0.8$ eV (Fig. 2b). Note that in Fig. 2c–f there are no odd parities for $+y$ and $-y$, i.e., $I(\mathbf{k}, E) \neq I(\mathcal{M}_y \mathbf{k}, E)$, where $\mathcal{M}_y \mathbf{k}$ is the mirror- y image of \mathbf{k} .

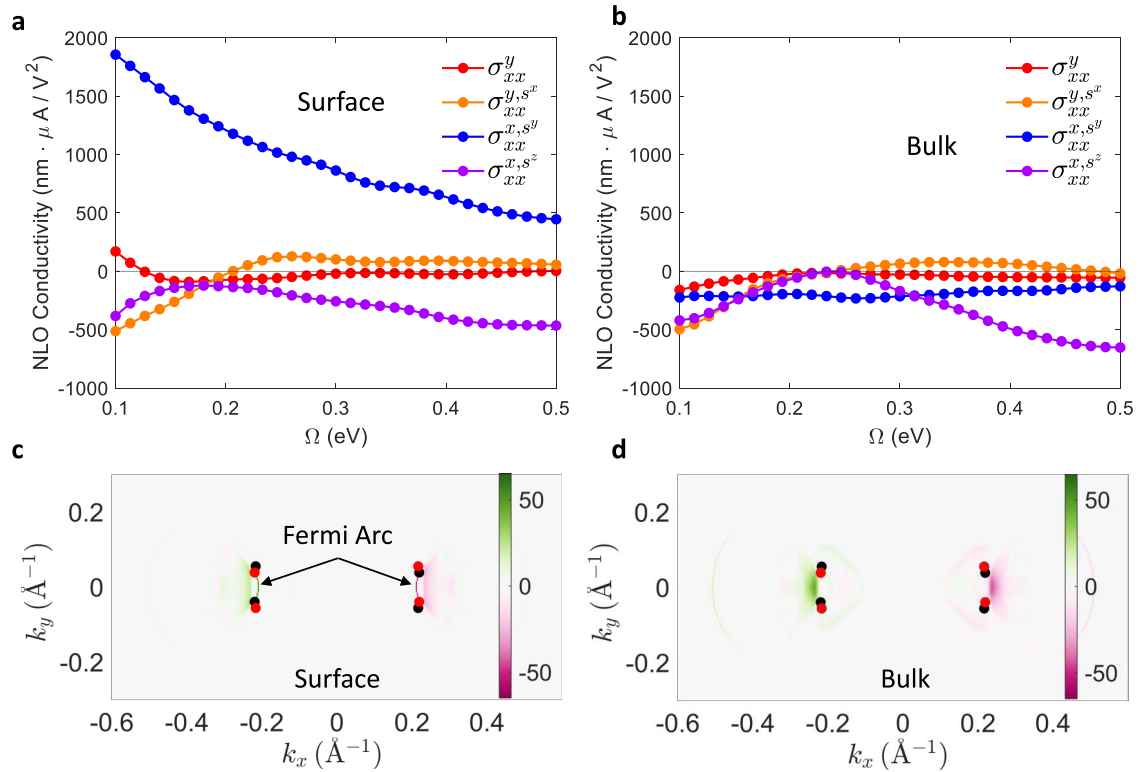


Fig. 3 BSPV conductivity for T_d -WTe₂. Nonzero elements of the conductivity tensor are shown for the (a) surface PL and (b) bulk PL. c, d Spin density of states, defined as $D_s^y(\mathbf{k}, E) = i\text{Tr}\{s^y [G_0^s(\mathbf{k}, E) - G_0^a(\mathbf{k}, E)]\}$ at $E = E_f$ for (c) surface PL and (d) bulk PL. In (c, d) the black and red dots to mark the locations of Weyl points with +1 and -1 chirality, respectively.

The surface responses can be influenced by non-topological surface effects as well, such as symmetry effect and surface spin-orbit coupling. The symmetry effect is the most prominent when the bulk has inversion symmetry. In this case, the second-order responses are only present on the surface and are forbidden in bulk. We also studied Au as an example to show how spin-orbit coupling can influence nonlinear optical response. As spin-orbit energy in Au is relatively large (around 0.5 eV per atom), it makes a non-negligible difference in the NLO responses for ω in the infrared range. To further distinguish the topological surface effects from trivial surface effects, we artificially strain T_d -WTe₂ so that it becomes topologically trivial. In this case, the differences between surface and bulk NLO are much less significant, indicating that the trivial surface effects, including symmetry effect and surface spin-orbit coupling, are minor in the case of T_d -WTe₂. Besides, we investigate topologically trivial materials such as 2H-MoS₂ and find that their $\sigma_{\text{PL}-0}$ and $\sigma_{\text{PL}-\infty}$ are generally close to each other (Supplementary Note 4). This again suggests the essential role of topological band effects. Finally, we would like to remark that topological surface effects have a significant impact on the NLO response, but it does not necessarily lead to opposite currents on the surface and in the bulk for all topological materials under all conditions (see Supplementary Fig. 18 for an example).

Bulk spin photovoltaic effect

Electrons have both charge and spin. When electrons move under light illumination, their charge degree of freedom leads to a DC charge current, which is the BPV effect discussed in the previous section. Concurrently, the spin degree of freedom leads to a DC spin current, which is called the bulk spin photovoltaic (BSPV) effect^{46,47}. BPV and BSPV are cousin processes and have similar physical origins. The microscopic mechanism of the BSPV can be explained in the following way: when electrons are pumped into the conduction bands by light, the spin-current operator $j^{a,s^i} =$

$\frac{1}{2}(v^a s^i + s^i v^a)$ for electrons on $+\mathbf{k}$ and $-\mathbf{k}$ would not cancel each other, and a net spin current can be generated. Here s^i is the spin operator. However, since spin is an axial vector, BPV and BSPV have very different selection rules under symmetry operations. This can be harnessed for the generation of pure spin current—the spin current is allowed by symmetry, while the charge current is forbidden⁴⁶. As each electron carries a charge of e and spin of $\frac{\hbar}{2}$, one may expect that in the sense of equivalency $\frac{\hbar}{2} = |e|$, BPV and BSPV should have similar magnitude. However, on the surface of topological materials such as T_d -WTe₂, BSPV can be stronger than BPV by a factor of 10, as we will show below. This makes the surfaces of topological materials ideal platforms for spintronics applications.

For spin current traveling in direction a with spin polarization i , we set the response operator θ in Eq. (1) as $j^{a,s^i} = \frac{1}{2}(v^a s^i + s^i v^a)$. The BSPV conductivity $\sigma_{bc}^{a,s^i}(0; \omega, -\omega)$ has a similar expression to the BPV conductivity σ_{bc}^a in Eq. (3) (Supplementary Note 2.1). Note that we divide σ_{bc}^{a,s^i} by $\frac{\hbar}{2e}$ so that it has the same unit as σ_{bc}^a . The mirror symmetry \mathcal{M}_x of T_d -WTe₂ forbids some elements of the B(S)PV conductivity tensor, such as σ_{xx}^x and σ_{xx}^{x,s^x} . This is because polar vectors such as \mathcal{E}_x, v_x flip sign under \mathcal{M}_x , while axial vectors such as s^x do not. Under linearly polarized light polarized in x -direction, the nonzero B(S)PV tensors are shown in Fig. 3a, b (we do not consider the current along the out-of-plane z -direction). A prominent feature is that σ_{xx}^{x,s^y} on the surface is almost ten times larger than its bulk counterpart, and is also ten times larger than other components such as σ_{xx}^{y,s^x} . Indeed, hundreds of nm·μA/V² are typical values for B(S)PV conductivities in typical topological materials and 2D materials^{29,46}, while σ_{xx}^{x,s^y} on PL-0 is as large as 2000 nm·μA/V² at $\omega = 0.1$ eV. This indicates that the spin current generation is exceptionally efficient on the surface of T_d -WTe₂. Such a strong spin current comes partially from the Rashba spin-orbit coupling on the surfaces. In Fig. 3c we plot the spin density

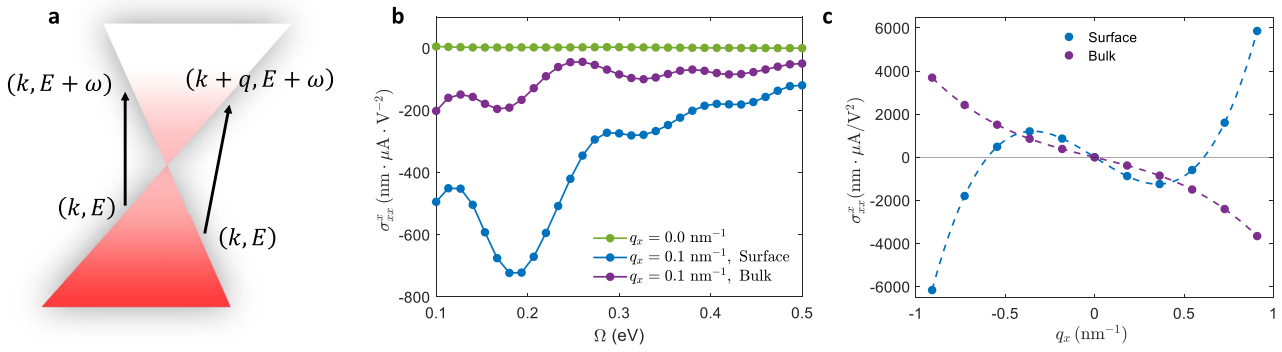


Fig. 4 BPV under inhomogeneous light field. **a** An illustration of the electron transitions under homogeneous (left arrow) and inhomogeneous (right arrow) field. **b** BPV conductivity under homogeneous ($\mathbf{q} = 0$) and inhomogeneous ($q_x \neq 0$) field. **c** The relationship between σ_{xx}^x ($\omega = 0.1 \text{ eV}$; q_x) and q_x for surface (blue curve) and bulk (purple curve) PL. The dashed curves are fittings of the solid dots with cubic functions.

of states of s^y (equivalent to the expectation value of s^y), defined as $D_{s^y}(\mathbf{k}, E) \equiv i\text{Tr}\{s^y [G_0^r(\mathbf{k}, E) - G_0^a(\mathbf{k}, E)]\}$ at $E = E_F$. One can see that spin- y polarization is stronger around the surface Fermi arc, while for \mathbf{k} -points distant from the Fermi arc, the spin- y polarization can be weaker. This suggests that BSPV is not solely determined by the spin polarization, but requires synergy with other factors, such as band velocities.

Inhomogeneous light field

In the visible or infrared range, the photon wavevector \mathbf{q} is much smaller than the size of the Brillouin zone, thus one usually sets $\mathbf{q} = 0$ when studying light-matter interactions. In other words, the light field is assumed to be homogeneous. However, the electromagnetic wave can be strongly inhomogeneous in the case of e.g., the Laguerre–Gaussian beam⁵⁷ with nonzero angular momentum. Subwavelength-scale variation can also be induced by plasmonic, polaritonic interactions^{58,59}. In these situations, the spatial variation of the light field is strong, and \mathbf{q} should not be neglected⁶⁰. In addition to these practical considerations, finite \mathbf{q} is also conceptually important, as it breaks certain spatial symmetries, and thus fundamentally alters the selection rules on optical process.

Our Green's function formalism provides a convenient way for incorporating the finite \mathbf{q} effect. Here we take the second-order BPV as an example. Under an inhomogeneous and oscillating electric field $\mathcal{E}(\omega, \mathbf{q})$ with frequency ω and wavevector \mathbf{q} , one has a spatially homogeneous and temporally static current, which is

$$\mathbf{j}^a = \sigma_{bc}^a(0; \omega, -\omega; \mathbf{q}, -\mathbf{q}) \mathcal{E}^b(\omega, \mathbf{q}) \mathcal{E}^c(-\omega, -\mathbf{q}), \quad (4)$$

where $\sigma_{bc}^a(0; \omega, -\omega; \mathbf{q}, -\mathbf{q})$ is the conductivity and can be calculated with the Green's function formalism (Supplementary Note 2.2). We will use $\sigma_{bc}^a(\omega, \mathbf{q}) \equiv \sigma_{bc}^a(0; \omega, -\omega; \mathbf{q}, -\mathbf{q})$ as a shorthand in the following. Intuitively, an electron in the state (\mathbf{k}, E) can (virtually) absorb momentum \mathbf{q} and energy ω from the inhomogeneous light field, jump to another state $(\mathbf{k} + \mathbf{q}, E + \omega)$, then return \mathbf{q} and ω to the light field and finally jump back to its original state (Fig. 4a). During this process, the electron may displace in real space, resulting in a charge current. Notably, \mathbf{q} identifies a preferred (or unique) direction for such a process, which could break certain spatial symmetries, including inversion, mirror, and rotation symmetries.

Td-WTe_2 has mirror symmetry \mathcal{M}_x . As a result, $\sigma_{xx}^x(\omega, \mathbf{q})$ must be zero when $\mathbf{q} = 0$ since it flips sign under \mathcal{M}_x . This is different from σ_{yy}^y studied in the previous sections, which can be non-zero even when $\mathbf{q} = 0$. In contrast, if $q_x \neq 0$, then $\sigma_{xx}^x(\omega, \mathbf{q})$ can be nonzero, which is vividly illustrated in Fig. 4b. As a comparison, we keep $q_x = 0$ and vary q_y , and $\sigma_{xx}^x(\omega, \mathbf{q})$ remains zero as expected

(Supplementary Fig. 17), since q_y cannot break \mathcal{M}_x . In Fig. 4c, we show how $\sigma_{xx}^x(\omega = 0.1 \text{ eV}; \mathbf{q})$ varies with q_x . Again, one can see that PLs on the surface and in the bulk have distinct behavior. $\sigma_{xx}^x(\omega, \mathbf{q})$ of the bulk PLs shows a cubic and monotonic relationship with q_x . In contrast, $\sigma_{xx}^x(\omega, \mathbf{q})$ on the surface is non-monotonic with q_x , and reverses direction at around $|q_x| \approx 0.6 \text{ nm}^{-1}$. This is somewhat surprising since $|q_x|$ determines the extent to which \mathcal{M}_x is broken, and one might expect that $\sigma_{xx}^x(\omega, \mathbf{q})$ should increase monotonically with q_x . The non-monotonic behavior can be understood intuitively in the following way. Two competing factors contribute to the magnitude of the NLO responses: (A) when $|\mathbf{q}|$ is large, spatial inhomogeneity of the light field is stronger. As a result, different electrons may have stronger tendencies to jump in the same (rather than the opposite) directions, which could result in a larger $\sigma_{xx}^x(\omega, \mathbf{q})$ when $|q_x|$ is large; (B) when $|\mathbf{q}|$ is large, the wavefunction overlap between (\mathbf{k}, E) and $(\mathbf{k} + \mathbf{q}, E + \omega)$ may be smaller, and the probability (transition rate) for a certain electron to jump between (\mathbf{k}, E) to $(\mathbf{k} + \mathbf{q}, E + \omega)$ may be smaller. This would result in a smaller $\sigma_{xx}^x(\omega, \mathbf{q})$ when $|q_x|$ is large. The competition between factors (A) and (B) can result in a non-monotonic relationship between $\sigma_{xx}^x(\omega, \mathbf{q})$ and q_x . In Supplementary Note 2.2, we give a more quantitative explanation of this effect.

Finally, we would like to remark that besides the inhomogeneous light field, a finite \mathbf{q} can also arise from inhomogeneous materials, which can be induced by e.g., strain gradient⁶¹ or heterostructures. Inhomogeneous light fields and materials should conceptually lead to similar results, although methodologically, the effect of inhomogeneous materials should be incorporated differently.

Higher-order response

Until now, we have been discussing the second-order optical responses, which scales as \mathcal{E}^2 . In recent years, higher-order responses have also attracted great interest^{34,62–65}, and efficient high-order responses have been demonstrated separately on the surface³⁴ and in the bulk⁶⁵ of topological materials. The higher-order responses can be distinct on the surface and in the bulk interior as well. Here we consider the third-order response, which can be characterized by the conductivity $\sigma_{bcd}^a(\omega_b + \omega_c + \omega_d; \omega_b, \omega_c, \omega_d)$ – that is, three electric fields $\mathcal{E}_b(\omega_b)$, $\mathcal{E}_c(\omega_c)$, $\mathcal{E}_d(\omega_d)$ with polarizations (b, c, d) and frequencies $(\omega_b, \omega_c, \omega_d)$ are coupled, and a current along direction a with frequency $\omega_b + \omega_c + \omega_d$ is generated. The detailed formula to calculate $\sigma_{bcd}^a(\omega_b, \omega_c, \omega_d)$ can be found in Supplementary Note 2.3.

Here we consider a simple but typical example of the third-order effect. When one applies two laser beams with

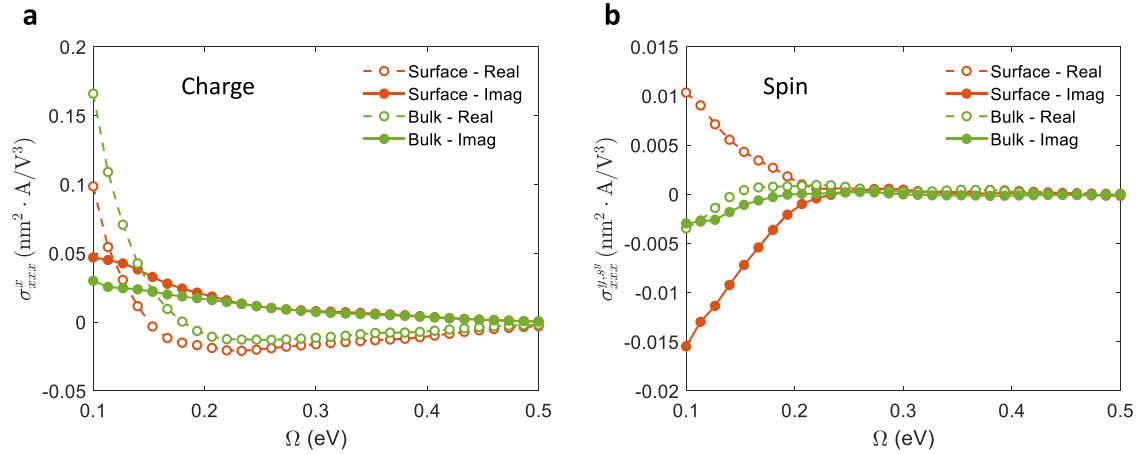


Fig. 5 Third-order conductivity of T_d -WTe $_2$, **a Charge current and **b** spin current. Red and green curves are for surface and bulk responses, respectively. Solid and dashed curves are the imaginary and real parts of the response functions, respectively.**

$\mathcal{E}_b = 2\tilde{\mathcal{E}}_b \cos(\omega t + \phi_b)$ and $\mathcal{E}_c = 2\tilde{\mathcal{E}}_c \cos(2\omega t + \phi_c)$, a static current j^a can be generated as

$$\begin{aligned} j^a &= \tilde{\mathcal{E}}_b^2 \tilde{\mathcal{E}}_c [\sigma_{bbc}^a(0; \omega, \omega, -2\omega) e^{i(2\phi_b - \phi_c)} + \sigma_{bbc}^a(0; -\omega, -\omega, 2\omega) e^{-i(2\phi_b - \phi_c)}] \\ &= \tilde{\mathcal{E}}_b^2 \tilde{\mathcal{E}}_c \text{Re}[\sigma_{bbc}^a(0; \omega, \omega, -2\omega) e^{i(2\phi_b - \phi_c)}], \end{aligned} \quad (5)$$

where we used $\sigma_{bbc}^a(0; \omega, \omega, -2\omega) = [\sigma_{bbc}^a(0; -\omega, -\omega, 2\omega)]^*$, which is a consequence of the time-reversal symmetry. We computed $\sigma_{xxx}^x(0; \omega, \omega, -2\omega)$ with the Green's function formalism, and the results are shown in Fig. 5a, where one can see that the third-order responses are distinct for the surface and the bulk as well. Moreover, $\sigma_{bbc}^a(0; \omega, \omega, -2\omega) \equiv e^{i\psi} |\sigma_{bbc}^a(0; \omega, \omega, -2\omega)|$ is a complex number, yielding $j^a = \tilde{\mathcal{E}}_b^2 \tilde{\mathcal{E}}_c |\sigma_{bbc}^a(0; \omega, \omega, -2\omega)| \cos(2\phi_b - \phi_c + \psi)$. Interestingly, since spin flips its direction under time-reversal symmetry, the spin current conductivity (Fig. 5b) satisfies $\sigma_{bbc}^{a,s}(0; \omega, \omega, -2\omega) = -[\sigma_{bbc}^{a,s}(0; -\omega, -\omega, 2\omega)]^*$, and the spin current obeys $j^{a,s} \propto \sin(2\phi_b - \phi_c + \psi_s)$, where ψ_s is the phase factor for the spin current. Therefore, the magnitude of both charge and spin current can be controlled by the phase difference $2\phi_b - \phi_c$. Furthermore, pure spin current without accompanying charge current can be generated when $2\phi_b - \phi_c + \psi = n\pi + \frac{\pi}{2}$, $n \in \mathbb{Z}$. These effects belong to the so-called two-color quantum interference control^{66–69}.

DISCUSSION

In this work, we used T_d -WTe $_2$ as an example to study the surface effects in NLO processes. The reason we choose T_d -WTe $_2$ is that the bulk of T_d -WTe $_2$ is non-centrosymmetric and semi-metallic, which is similar to the surface from a symmetry or bandgap point of view. Our results indicate that even in this case, the surface responses can still be drastically different from those in the bulk lattice. We clarify that this is mainly a topological effect, as topologically trivial materials do not give such drastic differences. This point is verified with both topologically trivial T_d -WTe $_2$ and 2H-MoS $_2$ (Supplementary Note 4).

As discussed before, in materials with inversion symmetry or nonzero bandgap, the difference between surface and bulk can be even more dramatic. In centrosymmetric materials, B(S)PV, as a second-order effect, is forbidden in the bulk interior. Therefore, under light illumination, the currents are purely on the surfaces, where the inversion symmetry is broken. As for topological insulators, the bulk has a finite bandgap and thus has no responses under light with below-bandgap frequencies (when the Fermi level

is in the bulk bandgap). However, the surface states are gapless and can have responses under light (in principle) arbitrarily low frequencies. These features are illustrated using Bi $_2$ Se $_3$ as an example (Supplementary Fig. 12). Note that in Bi $_2$ Se $_3$, the BPV conductivities on the top and bottom surfaces are opposite, thus the total current should be zero if the top and bulk surfaces are under the same light field. However, light with above-bulk-bandgap frequencies may not reach the bottom surface if the Bi $_2$ Se $_3$ is thick enough. In this case, the total current comes solely from the top surface and can be directly used to probe the surface states.

In conclusion, we have developed a generic Green's function framework for calculating the NLO properties, which can incorporate many-body effects beyond the single-particle approximation. As an example, we study the effect of strong electron-electron correlations represented by a Hubbard U term. In future works, we will use the Green's function framework to study NLO effects in other many-body systems. In this work, the Green's function framework is used to study the surfaces of topological materials, and it is found that under light illumination, the surface can behave distinctly from the bulk. Therefore, light can be used to probe the surface properties. On the other hand, when investigating the NLO properties of topological materials, the surface effects should be carefully considered, particularly when the light penetration depth is shallow, or the material has nanoscale dimensions. For example, in topological (semi-)metals, only tens of PLs (10–100 nm in thickness) may be active under light, and the surface effect can make a significant difference in the total responses (see Supplementary Note 6.1 for a quantitative estimation). This is important when using light as a probe of topological properties: the desired bulk properties may be obscured by surface effects, and the experimental results may deviate from theoretical predictions if the surface effects are not properly considered. Also, when searching for materials with large NLO responses for e.g., photodetection or energy harvesting purposes, it may be insufficient to look at only the bulk properties. The true responses can be obtained only when the surface and the bulk are both considered, and the surface can act either positively or negatively to the total response.

METHODS

Green's function formalism

Electrons in solid-state systems have interactions with e.g., phonons, defects, and other electrons. We call the electron system with these internal interactions the *base* system and assume that we have full knowledge of these base systems—we have their Green's functions G_0 in hand, which can either be rigorously calculated or be approximately obtained with e.g., perturbative expansions. External fields such as light illumination are treated as additional interactions, which can drive the

system out of equilibrium. Such external interactions are described by the self-energy terms Σ . The Green's functions with both internal and external interactions are denoted with G , which can be obtained from G_0 and Σ using Dyson's equation. Regarding the light-matter interaction, one has^{70,71} (Supplementary Note 1)

$$G^< = \left[\sum_{n=0}^{\infty} (G_0^< \Sigma^r)^n \right] G_0^< \left[\sum_{m=0}^{\infty} (\Sigma^a G_0^a)^m \right], \quad (6)$$

where $G_0^</math>/ G_0^a / $G_0^<$ are the retarded/advanced/lesser Green's function of the base system. $\Sigma^r(\mathbf{q}, \omega) = \Sigma^a(\mathbf{q}, \omega) = i\mathbf{e}\mathbf{v} \cdot \frac{\mathcal{E}}{\omega} e^{i(\mathbf{q}\cdot\mathbf{r} + \omega t)}$ is the retarded/advanced self-energy, where \mathbf{v} is the velocity matrix, while \mathcal{E} is the electric field with wavevector \mathbf{q} and frequency ω . Equations (1, 6) provide a systematic and convenient approach for computing the optical responses to an arbitrary order: for the N -th order optical response, one simply picks up all terms with $m + n = N$ in Eq. (6). The \mathbf{k} and E arguments are omitted in Eq. (6) for simplicity. Note that after each self-energy term $\Sigma^{r/a}(\mathbf{q}, \omega)$, the arguments \mathbf{k} and E should be shifted by \mathbf{q} and ω , respectively, corresponding to the momentum and energy conservation. When the base system is non-interacting, Eqs. (1) and (6) can be reduced to the common single-particle formula. This is verified theoretically and computationally in the Supplementary Note 1.3 and 1.4.$

Ab initio calculations

The ab initio calculations are based on density functional theory (DFT)^{72,73} as implemented in the Vienna ab initio simulation package (VASP)^{74,75}. Generalized gradient approximation (GGA) in the form of Perdew-Burke-Ernzerhof (PBE)⁷⁶ is used to treat the exchange-correlation interactions. Core and valence electrons are treated by projector augmented wave (PAW) method⁷⁷ and plane-wave basis functions, respectively. For DFT calculations of T_d -WTe₂, the first Brillouin zone is sampled by a $15 \times 9 \times 3$ \mathbf{k} -mesh. Then a tight-binding (TB) Hamiltonian is built from DFT results using the Wannier90 package⁷⁸ and is used to calculate the NLO responses within the Green's function framework. For the localized NLO responses on each PL, the BZ integration in Eq. (1) is carried out by \mathbf{k} -mesh sampling with $\int \frac{d\mathbf{k}}{(2\pi)^3} = \frac{1}{S} \sum_{\mathbf{k}} w_{\mathbf{k}}$, where S is the area of the 2D unit cell on each PL and $w_{\mathbf{k}}$ is the weight factor. For the NLO conductivity of common bulk materials, the \mathbf{k} -mesh sampling should be $\int \frac{d\mathbf{k}}{(2\pi)^3} = \frac{1}{V} \sum_{\mathbf{k}} w_{\mathbf{k}}$, where V is the volume of the 3D unit cell. Thus, the conductivities shown in this work differ from the common definition of conductivities by a factor L , which is the thickness of the unit cell. For the \mathbf{k} -integration in Eq. (1), a \mathbf{k} -mesh of 128×64 is used for T_d -WTe₂, while for the E -integration, a trapezoidal method is used with an energy interval of 10 meV. The convergence in both \mathbf{k} and E integrations is tested.

DATA AVAILABILITY

The authors declare that the main data supporting the findings of this study are available within the article and its Supplementary Information files.

CODE AVAILABILITY

The data that support the findings within this paper and the MATLAB code for calculating the shift and circular current conductivity are available from the corresponding authors upon reasonable request.

Received: 10 January 2022; Accepted: 5 April 2022;

Published online: 16 May 2022

REFERENCES

- Ma, J. et al. Nonlinear photoresponse of type-II Weyl semimetals. *Nat. Mater.* **18**, 476–481 (2019).
- Xu, H. et al. Colossal switchable photocurrents in topological Janus transition metal dichalcogenides. *npj Comput. Mater.* **7**, 1–9 (2021).
- Osterhoudt, G. B. et al. Colossal mid-infrared bulk photovoltaic effect in a type-I Weyl semimetal. *Nat. Mater.* **18**, 471–475 (2019).
- Zhang, Y. & Fu, L. Terahertz detection based on nonlinear Hall effect without magnetic field. *Proc. Natl. Acad. Sci.* **118** (2021).
- Qin, M., Yao, K. & Liang, Y. C. High efficient photovoltaics in nanoscaled ferroelectric thin films. *Appl. Phys. Lett.* **93**, 122904 (2008).
- Choi, T., Lee, S., Choi, Y. J., Kiryukhin, V. & Cheong, S. W. Switchable ferroelectric diode and photovoltaic effect in BiFeO₃. *Science* **324**, 63–66 (2009).
- Yang, S. Y. et al. Above-bandgap voltages from ferroelectric photovoltaic devices. *Nat. Nanotechnol.* **5**, 143–147 (2010).
- Daranciang, D. et al. Ultrafast photovoltaic response in ferroelectric nanolayers. *Phys. Rev. Lett.* **108**, 087601 (2012).
- Grinberg, I. et al. Perovskite oxides for visible-light-absorbing ferroelectric and photovoltaic materials. *Nature* **503**, 509–512 (2013).
- Bhatnagar, A., Roy Chaudhuri, A., Heon Kim, Y., Hesse, D. & Alexe, M. Role of domain walls in the abnormal photovoltaic effect in BiFeO₃. *Nat. Commun.* **4**, 1–8 (2013).
- Xu, S.-Y. et al. Electrically switchable Berry curvature dipole in the monolayer topological insulator WTe₂. *Nat. Phys.* **14**, 900–906 (2018).
- Ma, Q. et al. Direct optical detection of Weyl fermion chirality in a topological semimetal. *Nat. Phys.* **13**, 842–847 (2017).
- Xu, S.-Y. et al. Spontaneous gyrotropic electronic order in a transition-metal dichalcogenide. *Nature* **578**, 545–549 (2020).
- Kaplan, D., Holder, T. & Yan, B. Nonvanishing subgap photocurrent as a probe of lifetime effects. *Phys. Rev. Lett.* **125**, 227401 (2020).
- Ahn, J., Guo, G.-Y. & Nagaosa, N. Low-frequency divergence and quantum geometry of the bulk photovoltaic effect in topological semimetals. *Phys. Rev. X* **10**, 041041 (2020).
- Holder, T., Kaplan, D. & Yan, B. Consequences of time-reversal-symmetry breaking in the light-matter interaction: berry curvature, quantum metric, and diabatic motion. *Phys. Rev. Res.* **2**, 033100 (2020).
- Watanabe, H. & Yanase, Y. Chiral photocurrent in parity-violating magnet and enhanced response in topological antiferromagnet. *Phys. Rev. X* **11**, 011001 (2021).
- Liu, J., Xia, F., Xiao, D., García de Abajo, F. J. & Sun, D. Semimetals for high-performance photodetection. *Nat. Mater.* **19**, 830–837 (2020).
- Ma, Q., Grushin, A. G. & Burch, K. S. Topology and geometry under the nonlinear electromagnetic spotlight. *Nat. Mater.* **20**, 1601–1614 (2021).
- Tan, L. Z. & Rappe, A. M. Enhancement of the bulk photovoltaic effect in topological insulators. *Phys. Rev. Lett.* **116**, 237402 (2016).
- Xu, H., Zhou, J., Wang, H. & Li, J. Giant photonic response of Mexican-Hat topological semiconductors for mid-infrared to terahertz applications. *J. Phys. Chem. Lett.* **11**, 6119–6126 (2020).
- De Juan, F., Grushin, A. G., Morimoto, T. & Moore, J. E. Quantized circular photogalvanic effect in Weyl semimetals. *Nat. Commun.* **8**, 1–7 (2017).
- Chan, C.-K., Lindner, N. H., Refael, G. & Lee, P. A. Photocurrents in Weyl semimetals. *Phys. Rev. B* **95**, 041104 (2017).
- Ni, Z. et al. Linear and nonlinear optical responses in the chiral multifold semimetal RhSi. *npj Quantum Mater.* **5**, 96 (2020).
- Ni, Z. et al. Giant topological longitudinal circular photo-galvanic effect in the chiral multifold semimetal CoSi. *Nat. Commun.* **12**, 154 (2021).
- Morimoto, T. & Nagaosa, N. Topological nature of nonlinear optical effects in solids. *Sci. Adv.* **2**, e1501524 (2016).
- Fei, R., Song, W. & Yang, L. Giant linearly-polarized photogalvanic effect and second harmonic generation in two-dimensional axion insulators. *Phys. Rev. B* **102**, 035440 (2020).
- Wu, L. et al. Giant anisotropic nonlinear optical response in transition metal monpnictide Weyl semimetals. *Nat. Phys.* **13**, 350–355 (2017).
- Xu, Q. et al. Comprehensive scan for nonmagnetic Weyl semimetals with nonlinear optical response. *npj Comput. Mater.* **6**, 1–7 (2020).
- Hosur, P. Circular photogalvanic effect on topological insulator surfaces: berry-curvature-dependent response. *Phys. Rev. B* **83**, 035309 (2011).
- Braun, L. et al. Ultrafast photocurrents at the surface of the three-dimensional topological insulator Bi₂Se₃. *Nat. Commun.* **7**, 13259 (2016).
- Chang, G. et al. Unconventional photocurrents from surface fermi arcs in topological chiral semimetals. *Phys. Rev. Lett.* **124**, 166404 (2020).
- Kim, K. W., Morimoto, T. & Nagaosa, N. Shift charge and spin photocurrents in Dirac surface states of topological insulator. *Phys. Rev. B* **95**, 035134 (2017).
- Giorgianni, F. et al. Strong nonlinear terahertz response induced by Dirac surface states in Bi₂Se₃ topological insulator. *Nat. Commun.* **7**, 11421 (2016).
- Hsieh, D. et al. Nonlinear optical probe of tunable surface electrons on a topological insulator. *Phys. Rev. Lett.* **106**, 057401 (2011).
- Junck, A., Refael, G. & Von Oppen, F. Photocurrent response of topological insulator surface states. *Phys. Rev. B* **88**, 075144 (2013).
- Dai, Z., Schankler, A. M., Gao, L., Tan, L. Z. & Rappe, A. M. Phonon-assisted ballistic current from first-principles calculations. *Phys. Rev. Lett.* **126**, 177403 (2021).
- Ishizuka, H. & Nagaosa, N. Theory of bulk photovoltaic effect in Anderson insulator. *Proc. Natl. Acad. Sci.* **118**, 2021 (2021).
- Chan, Y.-H., Qiu, D. Y., Jornada, F. Hda & Louie, S. G. Giant exciton-enhanced shift currents and direct current conduction with subbandgap photo excitations produced by many-electron interactions. *Proc. Natl. Acad. Sci.* **118**, 2021 (2021).

40. Trolle, M. L., Seifert, G. & Pedersen, T. G. Theory of excitonic second-harmonic generation in monolayer MoS_2 . *Phys. Rev. B* **89**, 235410 (2014).
41. Kaneko, T., Sun, Z., Murakami, Y., Golež, D. & Millis, A. J. Bulk photovoltaic effect driven by collective excitations in a correlated insulator. *Phys. Rev. Lett.* **127**, 127402 (2020).
42. Sancho, M. P. L., Sancho, J. M. L. & Rubio, J. Quick iterative scheme for the calculation of transfer matrices: application to Mo (100). *J. Phys. F. Met. Phys.* **14**, 1205 (1984).
43. Sancho, M. P. L., Sancho, J. M. L., Sancho, J. M. L. & Rubio, J. Highly convergent schemes for the calculation of bulk and surface Green functions. *J. Phys. F. Met. Phys.* **15**, 851 (1985).
44. Soluyanov, A. A. et al. Type-II Weyl semimetals. *Nature* **527**, 495–498 (2015).
45. Li, P. et al. Evidence for topological type-II Weyl semimetal WTe₂. *Nat. Commun.* **8**, 2150 (2017).
46. Xu, H., Wang, H., Zhou, J. & Li, J. Pure spin photocurrent in non-centrosymmetric crystals: bulk spin photovoltaic effect. *Nat. Commun.* **12**, 4330 (2021).
47. Mu, X., Pan, Y. & Zhou, J. Pure bulk orbital and spin photocurrent in two-dimensional ferroelectric materials. *npj Comput. Mater.* **7**, 61 (2021).
48. Mahan, G. D. *Many-Particle Physics*. (Springer US, 2000).
49. Wang, Q. et al. Room-temperature nanoseconds spin relaxation in WTe₂ and MoTe₂ thin films. *Adv. Sci.* **5**, 1700912 (2018).
50. Liang, T. et al. Ultrahigh mobility and giant magnetoresistance in the Dirac semimetal Cd₃As₂. *Nat. Mater.* **14**, 280–284 (2015).
51. Shekhar, C. et al. Extremely large magnetoresistance and ultrahigh mobility in the topological Weyl semimetal candidate NbP. *Nat. Phys.* **11**, 645–649 (2015).
52. Wang, H., Zhang, C. & Rana, F. Surface recombination limited lifetimes of photoexcited carriers in few-layer transition metal dichalcogenide MoS₂. *Nano Lett.* **15**, 8204–8210 (2015).
53. Niehues, I. et al. Strain control of exciton-phonon coupling in atomically thin semiconductors. *Nano Lett.* **18**, 1751–1757 (2018).
54. Georges, A., Kotliar, G., Krauth, W. & Rozenberg, M. J. Dynamical mean-field theory of strongly correlated fermion systems and the limit of infinite dimensions. *Rev. Mod. Phys.* **68**, 13 (1996).
55. Kotliar, G. et al. Electronic structure calculations with dynamical mean-field theory. *Rev. Mod. Phys.* **78**, 865–951 (2006).
56. Singh, V. et al. DMFTwDFT: an open-source code combining Dynamical Mean Field Theory with various density functional theory packages. *Comput. Phys. Commun.* **261**, 107778 (2021).
57. Allen, L., Beijersbergen, M. W., Spreeuw, R. J. C. & Woerdman, J. P. Orbital angular momentum of light and the transformation of Laguerre-Gaussian laser modes. *Phys. Rev. A* **45**, 8185 (1992).
58. Lezec, H. J. et al. Beaming light from a subwavelength aperture. *Science* **297**, 820–822 (2002).
59. Barnes, W. L., Dereux, A. & Ebbesen, T. W. Surface plasmon subwavelength optics. *Nature* **424**, 824–830 (2003).
60. Ji, Z. et al. Spatially dispersive circular photogalvanic effect in a Weyl semimetal. *Science* **18**, 955–962 (2019).
61. Feng, J., Qian, X., Huang, C.-W. & Li, J. Strain-engineered artificial atom as a broad-spectrum solar energy funnel. *Nat. Photonics* **6**, 866–872 (2012).
62. Hafez, H. A. et al. Extremely efficient terahertz high-harmonic generation in graphene by hot Dirac fermions. *Nature* **561**, 507–511 (2018).
63. Tancogne-Dejean, N. & Rubio, A. Atomic-like high-harmonic generation from two-dimensional materials. *Sci. Adv.* **4**, eaao5207 (2018).
64. Fregoso, B. M., Muniz, R. A. & Sipe, J. E. Jerk current: a novel bulk photovoltaic effect. *Phys. Rev. Lett.* **121**, 176604 (2018).
65. Cheng, B. et al. Efficient terahertz harmonic generation with coherent acceleration of electrons in the Dirac semimetal Cd_3As_2 . *Phys. Rev. Lett.* **124**, 117402 (2020).
66. Atanasov, R., Haché, A., Hughes, J. L. P., Driel, H. M. van & Sipe, J. E. Coherent control of photocurrent generation in bulk semiconductors. *Phys. Rev. Lett.* **76**, 1703 (1996).
67. Haché, A. et al. Observation of coherently controlled photocurrent in unbiased Bulk GaAs. *Phys. Rev. Lett.* **78**, 306 (1997).
68. Stevens, M. J. et al. Quantum interference control of ballistic pure spin currents in semiconductors. *Phys. Rev. Lett.* **90**, 136603 (2003).
69. Zhao, H., Loren, E. J., van Driel, H. M. & Smirl, A. L. Coherence control of hall charge and spin currents. *Phys. Rev. Lett.* **96**, 246601 (2006).
70. Parker, D. E., Morimoto, T., Orenstein, J. & Moore, J. E. Diagrammatic approach to nonlinear optical response with application to Weyl semimetals. *Phys. Rev. B* **99**, 045121 (2019).
71. João, S. M. & Lopes, J. M. V. P. Basis-independent spectral methods for nonlinear optical response in arbitrary tight-binding models. *J. Phys. Condens. Matter* **32**, 125901 (2019).
72. Hohenberg, P. & Kohn, W. Inhomogeneous electron gas. *Phys. Rev.* **136**, B864–B871 (1964).
73. Kohn, W. & Sham, L. J. Self-consistent equations including exchange and correlation effects. *Phys. Rev.* **140**, A1133–A1138 (1965).
74. Kresse, G. & Furthmüller, J. Efficiency of ab-initio total energy calculations for metals and semiconductors using a plane-wave basis set. *Comput. Mater. Sci.* **6**, 15–50 (1996).
75. Kresse, G. & Furthmüller, J. Efficient iterative schemes for ab initio total-energy calculations using a plane-wave basis set. *Phys. Rev. B* **54**, 11169–11186 (1996).
76. Perdew, J. P., Burke, K. & Ernzerhof, M. Generalized gradient approximation made simple. *Phys. Rev. Lett.* **77**, 3865–3868 (1996).
77. Blöchl, P. E. Projector augmented-wave method. *Phys. Rev. B* **50**, 17953–17979 (1994).
78. Mostofi, A. A. et al. An updated version of wannier90: a tool for obtaining maximally-localised Wannier functions. *Comput. Phys. Commun.* **185**, 2309–2310 (2014).

ACKNOWLEDGEMENTS

This work was supported by an Office of Naval Research MURI through grant #N00014-17-1-2661. The authors acknowledge helpful discussions with Jian Zhou.

AUTHOR CONTRIBUTIONS

H.X. and J.L. conceived the idea and designed the project. H.X. derived the theories. H.X. performed the calculations and wrote the paper with the help of H.W. and J.L. J.L. supervised the project. All authors analyzed the data and contributed to the discussions of the results.

COMPETING INTERESTS

The authors declare no competing interests.

ADDITIONAL INFORMATION

Supplementary information The online version contains supplementary material available at <https://doi.org/10.1038/s41524-022-00782-y>.

Correspondence and requests for materials should be addressed to Ju Li.

Reprints and permission information is available at <http://www.nature.com/reprints>

Publisher's note Springer Nature remains neutral with regard to jurisdictional claims in published maps and institutional affiliations.



Open Access This article is licensed under a Creative Commons Attribution 4.0 International License, which permits use, sharing, adaptation, distribution and reproduction in any medium or format, as long as you give appropriate credit to the original author(s) and the source, provide a link to the Creative Commons license, and indicate if changes were made. The images or other third party material in this article are included in the article's Creative Commons license, unless indicated otherwise in a credit line to the material. If material is not included in the article's Creative Commons license and your intended use is not permitted by statutory regulation or exceeds the permitted use, you will need to obtain permission directly from the copyright holder. To view a copy of this license, visit <http://creativecommons.org/licenses/by/4.0/>.

© The Author(s) 2022